CFD analysis of Hydrodynamic Characteristics of Tidal Current Turbines

Ai Choong Loh
SHEVS IFT Consultants Pte Ltd 12 Lor Bakar Batu, #05-11, Singapore 348745
loh_lacer@hotmail.com

Ooi Yongson
Centre for Advanced Mechanical and Green Technology, Faculty of Engineering and Technology, Multimedia University, Bukit Beruang, 75450 Malacca, Malaysia
yongson.ooi@mmu.edu.my

Lingenthiran Samylingam
Centre for Advanced Mechanical and Green Technology, Faculty of Engineering and Technology, Multimedia University, Jalan Ayer Keroh Lama, Bukit Beruang, 75450 Melaka, Malaysia
lingenthiran@mmu.edu.my

Dirk Rilling
Centre for Advanced Mechanical and Green Technology, Faculty of Engineering and Technology, Multimedia University, Bukit Beruang, 75450 Malacca, Malaysia
d.rilling@me.com

Chee Kuang Kok
Centre for Advanced Mechanical and Green Technology, Faculty of Engineering and Technology, Multimedia University, Bukit Beruang, 75450 Malacca, Malaysia
ckkok@mmu.edu.my

Gooi Mee Chen
Centre for Advanced Mechanical and Green Technology, Faculty of Engineering and Technology, Multimedia University, Bukit Beruang, 75450 Malacca, Malaysia
gmchen@mmu.edu.my (corresponding author)

Received: 16 October 2024 | Revised: 19 November 2024 | Accepted: 1 December 2024

 DOI: https://doi.org/10.48084/etasr.9293

ABSTRACT

Malaysia uses mostly fossil fuels for electricity generation. This study examines the hydrodynamic performance of tidal turbines, especially designed for three sites in East Malaysia: Sibu, Kota Belud, and Pulau Jambongan. The performance characteristics of these site-specific turbines were analyzed with the use of Computational Fluid Dynamics (CFD) and were validated with experimental benchmarks. The results indicate that a power coefficient greater than 0.4 is possible at Tip Speed Ratios (TSR) between 4 and 7, with the best performance recorded at TSR 5 for inflow velocities between 0.75 and 1.35 m/s. This study highlights the potential of tidal energy as a sustainable resource for Malaysia and provides a basis for further development in the region.

Keywords-CFD; hydrodynamic performance; Tidal Current Turbine (TCT); renewable energy

I. INTRODUCTION

TCTs have gained considerable attention as a viable solution in the search for sustainable energy sources. Underwater or marine turbines, are engineered devices designed to capture the kinetic energy present in tidal currents, and subsequently convert it into electrical energy [1, 2]. Authors in [3] mention that locations with strong tidal currents,

such as coastal locations in East Malaysia, provide favorable conditions for the application of this promising technology. Tidal energy has gained worldwide attention as a reliable renewable energy source. Countries, such as the United Kingdom, Canada, and South Korea, have made significant investments in tidal energy projects, with advances in turbine technology and energy storage improving the technical and economic capability of large-scale projects [4]. The global push for carbon reduction has positioned tidal energy as an appealing alternative, particularly in regions with strong tidal currents. Given Malaysia's unique geographical conditions, using tidal energy offers a promising opportunity of reducing dependence on fossil fuels [5]. The unique geographical characteristics of East Malaysia, including its proximity to the South China Sea and the Sulu Sea, makes it a favorable location for using tidal energy through the installation of TCT. Authors in [3] found three possible sites, namely Pulau Jambongan, Kota Belud, and Sibu, which could generate 8604 GWh/year of energy, assuming turbines with a power coefficient of 0.4. The use of the TCTs in East Malaysia offers a promising opportunity to effectively meet the energy needs of the region [6]. The analysis of the hydrodynamic performance of TCTs is of great importance in the field of marine renewable energy [7]. It is necessary to understand and improve this efficacy, in order to maximize energy extraction and ensure the long-term viability of tidal energy systems, considering the fluid dynamics and their effect on the surrounding marine ecosystem [8]. The turbine's design, the geometry and the number of its blades [9], the materials used in its construction, how it is placed within the tidal current, and the hydrofoil profile, are important for the attribution of the TCTs. Tidal turbine technology deploys the Blade Element Momentum Theory (BEMT) for turbine design, similar to its application in wind turbine technology. Authors in [10] utilized the BEMT methodology to develop a laboratory scale tidal turbine design. This research highlighted the importance of conducting an experimental investigation to validate the established turbine simulation codes. Authors in [11] developed a 1 MW TCT for the southwest coast of Korea, which was based on BEMT. This study focuses on the advancement of the hydrofoil and blade design, with particular emphasis on reduced chord length. Authors in [12] developed a mathematical model to predict the hydrodynamic efficiency of a tidal stream turbine under non-uniform tidal inflow conditions. Authors in [13] implemented an analytical wake model to estimate the characteristics of a tidal stream turbine under various turbulent scenarios. Authors in [14] developed a BEMT model specifically designed to simulate vertical axis tidal turbine rotors with high strength and high loads. This model addresses the limitations of traditional BEMT models in accurately representing such rotors. The model accurately reproduced peak efficiency values with a maximum deviation of 2.5% for a low solidity wind turbine, 8% for a high solidity wind turbine, and 10% for a high solidity tidal turbine in confined flow.

Authors in [15] applied the BEMT model to predict and evaluate the efficiency of a scaled turbine in both a flume and a towing tank. The analysis was performed numerically and experimentally for a turbine operating at flow velocities of 0.5 m/s and 1.0 m/s, wave amplitudes of 0.2 m and 0.4 m, and wave durations of 1.5 s and 1.7 s, and concluded to a remarkable level of agreement between the numerical model and the experimental study. However, at low TSRs, the model tends to underestimate the thrust and the range between the highest and lowest values obtained in the experiments. Authors in [16] employed two methods to generate synthetic turbulence: the synthetic vortex method and the spectral Sandia method. A robust BEMT model, derived from the classical formulation of the BEMT, was used to predict the response of the Tidal Energy Converter (TEC) to synthetic turbulence. The variability of the TEC load is lower during stall operation than at higher tip speed ratios. The variability of the turbine loads is directly related to the level of turbulence in the incoming flow. Authors in [17] recently derived and proved that the rotor design method converges for all reasonable model inputs. The study compared these optimal rotor designs with those of a nonlinear programming algorithm to verify the design method. A great number of numerical experiments yielded relative chord and twist profile errors of less than 13% and 5%, respectively, and efficiency, thrust, torque, and power coefficients of less than 0.3%. The design method computed optimal designs 170 times faster than nonlinear programming. Based on these results, they proposed a new rotor design method to aid in the conceptual design of rotorcraft. Authors in [18] used a detailed flow analysis to explain what physical mechanisms are missing from Technology Readiness Level (TRL) and Stall Delay (SD) corrections and proposed an improvement to the Prandtl model. The corrections were compared with the RANS CFD simulations of the NREL 5 MW rotor at the design TSRs, TSR 4, and TSR 10. At TSR 10, the Prandtl TLC loads are 5%-15% higher than CFD. A lower downwash angle of attack overestimates the lift coefficient by 5%-10%. The Eggers SD correction predicts an incorrect drag coefficient at TSR 4, but the lift coefficient matches better. Authors in [19] used the BEM method to calculate the aerodynamic performance of horizontal-axis wind turbine blades. No aerodynamic interaction was assumed in the blade analysis, which includes several computational elements, such as blade tip radius, blade twist, lift-drag ratio, and induction factors as the main dynamic variables affecting the performance of the wind blade. The selected wind turbine generates 3739.5 N, 1827.0 Nm, and 29.9 kW of thrust, torque, and power, respectively. They also reported that reducing the number of blade elements underestimates the aerodynamic predictions, therefore, the BEM equations must be carefully selected. The radial differential power of the wind turbine span peaks at r/R=0.8. The BEM and other modeling methods are effective for design and analysis [20-23]. BEM methods analyze the aerodynamic performance of wind turbines, but validation is needed to verify the results [24]. Authors in [25] discussed the BEM validation methods for wind turbine aerodynamic analysis. They concluded that when validated against experimental data and other advanced models, such as higher-order vortex and CFD models, their results were highly accurate. However, they emphasized that experimental data are needed for wind turbine studies to understand aerodynamic mechanisms and validate models. The objective of this study is to examine the hydrodynamic efficiency of turbines designed for three specific locations in East Malaysia, namely Pulau Jambongan, Kota Belud and Sibu, considering the tidal

velocity and accessible depths at each location. This objective will be achieved by using a CFD code, which will be compared with the results of a previous experimental study [10]. Through a comprehensive analysis of the interaction between the technology and the unique characteristics of tidal currents in East Malaysia, the results of this study will provide significant knowledge that can be used to enhance the development and operation of effective and environmentally friendly tidal energy systems in the area. In addition, the results of this study have the potential to move East Malaysia towards a more environmentally sustainable and resilient energy future.

II. TURBINE DESIGNS OF SIBU, KOTA BELUD AND PULAU JAMBONGAN

In the BEMT, a tidal turbine of length R is divided into several sections, and the profile is described by the section pitch angle and its chord length distribution across the turbine. The blade section pitch angle θ_P, and the corresponding chord length c, determined from the literature, are functions of the relative wind angle φ, the angle of attack α, the distance of the section profile from the blade root r, the length of the turbine R, the tip speed ratio TSR, the number of blades, and the lift coefficient, C_l [26]. In this study, the length of the blade R, is estimated under the assumption that the blades cannot penetrate the upper 7 m of the depth and 0.25 H from the bottom, where H is defined as the depth of the sea [27]. The nominal sea depth at the three Malaysian sites, H, was estimated in [3] using the Princeton Ocean Model. In addition, the TSR is chosen to be 5.5, which is within the range limit in the literature. In wind turbine technology, the chosen TSR is always between 4 and 10 [26]. In contrast, authors in [27] reported that in ocean current turbine technology, cavitation tends to occur when the TSR is greater than 7. The NACA 6 series airfoils, ranging from 63812 to 63824, are selected in this study in light of the research conducted in [28], which indicates that the NACA 6 series airfoil, particularly 63--8xx, exhibits better performance by allowing a wider range of lift coefficients without the occurrence of cavitation. The angle of attack and lift coefficient in this study are calculated based on the performance characteristics of the NACA 63815 [28] and presented in Table I. NACA 63815 at 0.75 R is taken as the base profile for the lift coefficient value. Table II shows that the 6-degree angle of attack has the lowest ratio of drag coefficient to lift coefficient, with an estimated lift coefficient of 1.05.

TABLE I. PERFORMANCE CHARACTERISTICS OF NACA 63815

Attack angle (°)	**Lift coefficient C_l**	**Drag coefficient C_d**	**C_d/C_l**
2	0.73	0.025	0.0345
3	0.80	0.028	0.0350
4	0.85	0.030	0.0353
5	0.90	0.032	0.0356
6	1.05	0.034	0.0324
7	1.10	0.040	0.0364
8	1.20	0.052	0.0433
9	1.25	0.065	0.0520
10	1.30	0.080	0.0615

The chord length and twist angles of each section are then calculated, and Table II depicts the profiles of the designed turbine blades for different locations in East Malaysia, while Figure 1 illustrates the CAD model of the designed blade.

III. NUMERICAL MODEL SETUP

A. Computational Domain and Discretization

Under the assumption of uniform inflow and symmetric positioning of the turbine blades, the numerical analysis is performed on only one third of the fluid domain, which represents a single blade, and ANSYS CFX is used to model the problem in this study.

TABLE II. DESIGNED TURBINE PROFILES

Angle of attack (°)								
r/*R*	Section radius *r* (m)			Angle of wind, φ (°)	Section pitch angle, θ_P (°)	Section chord *c* (m)		
	9 (m)	15 (m)	30 (m)			9 (m)	15 (m)	30 (m)
0.2	1.8	3	6	28.18	22.18	1.70	2.84	5.68
0.25	2.25	3.75	7.5	24.02	18.02	1.55	2.59	5.18
0.3	2.7	4.5	9	20.81	14.81	1.41	2.34	4.69
0.35	3.15	5.25	10.5	18.30	12.30	1.27	2.12	4.24
0.4	3.6	6	12	16.30	10.30	1.15	1.92	3.85
0.45	4.05	6.75	13.5	14.67	8.67	1.05	1.75	3.51
0.5	4.5	7.5	15	13.32	7.32	0.97	1.61	3.22
0.55	4.95	8.25	16.5	12.20	6.20	0.89	1.49	2.97
0.6	5.4	9	18	11.24	5.24	0.83	1.38	2.75
0.65	5.85	9.75	19.5	10.42	4.42	0.77	1.28	2.56
0.7	6.3	10.5	21	9.71	3.71	0.72	1.20	2.40
0.75	6.75	11.25	22.5	9.08	3.08	0.68	1.13	2.25
0.8	7.2	12	24	8.54	2.54	0.64	1.06	2.12
0.85	7.65	12.75	25.5	8.05	2.05	0.60	1.00	2.00
0.9	8.1	13.5	27	7.61	1.61	0.57	0.95	1.90
0.95	8.55	14.25	28.5	7.22	1.22	0.54	0.90	1.80
1	9	15	30	6.87	0.87	0.52	0.86	1.72

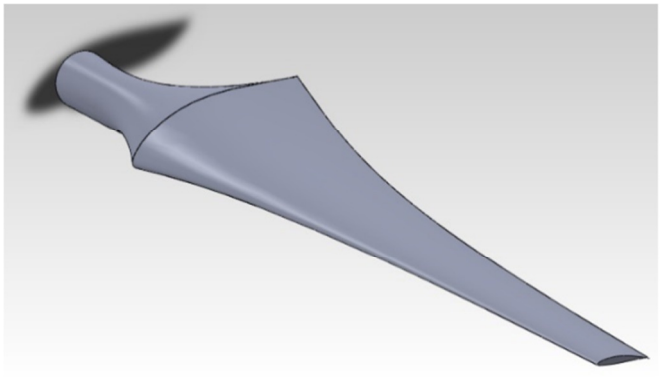

Fig. 1. CAD model of the designed blade.

The computational domain in the present case can be divided into two parts: an inner rotating part with the turbine blade and hub, and a stationary outer part consisting of the inlet, outlet, and far-field, as shown in Figures 2 (a) and 2 (b). Authors in [29] reported that grid expansion in the flow directions of 4 R upstream, 4 R downstream of the turbine, and 3 R in the spanwise direction can ensure an undisturbed flow field near the domain boundaries, and the size of the computational domain in this study is set to 11.5 R in length and 4.5 R in radius, where R is the length of the turbine blade. The blade is located 4 R from the inlet, and thus 7.5 R from the outlet for wake development. The inner rotating domain,

located 3 R from the inlet, has a length of 3.75 *R* and a radius of 1.75 *R*. The use of the rotating domain computes the flow field around the turbine blade by freezing the blade while solving the flow field using the rotating reference frame. The computational domain is discretized by creating grids to form meshes. The blade surfaces are meshed with quadrilateral cells, while the other surfaces are meshed with triangular cells, as evidenced in Figures 2 (c) and 2 (d). At the boundary layer, the meshes are denser compared to the rest of the fluid domain. The mesh elements in the boundary layer are hexahedral, and Figure 2 (e) shows an enlarged boundary layer mesh. Tetrahedral elements are applied to the rest of the fluid domain, as portrayed in Figure 2 (f). The size of the tetrahedral meshes is controlled by the value of the boundary decay, which qualitatively controls the effect of the boundary cell size on the interior cell size.

B. Mesh Independence Study

The mesh independence study is performed by comparing the simulation results with the literature experimental results at TSR 5 [30]. The power coefficients of the experimental data at TSR 5 are in the range of 0.44-0.45, corresponding to torques in the range of 9 Nm -9.3 Nm. The torque value is in the range of published experimental results with blade surface mesh pitch of 375 × 45 × 60 and 500 × 60 × 60. Since the results are approximately the same for both sizes, 375 × 45 × 60 is selected because the number of mesh elements is relatively small [31]. A detailed study of mesh independence is necessary to ensure that the chosen mesh provides accurate results while maintaining computational efficiency [32]. Three mesh configurations were tested with different numbers of elements and levels of refinement: a coarse mesh (250 × 30 × 60), an intermediate mesh (375 × 45 × 60), and a fine mesh (500 × 60 × 60). The results from the intermediate and fine meshes exhibited minimal variation in key outputs, such as torque and power coefficients, indicating convergence, as presented in Table III. The intermediate mesh was ultimately selected because it provided an optimal balance of accurately capturing flow characteristics while reducing computational requirements. This mesh configuration ensured the reliability of the results within an acceptable tolerance range, which was validated by a comparison with the experimental benchmark data.

C. Governing Equations and Boundary Conditions

The set of governing equations solved in the computation for an incompressible, turbulent, and isothermal flow is the unsteady conservative form of the Reynolds Averaged Navier-Stokes (RANS) equations, which consists of the continuity, momentum, and turbulence equations, respectively [31]:

$$\frac{\partial u_j}{\partial x_j} = 0 \quad (1)$$

$$\frac{\partial}{\partial t}(\rho u_j) + \frac{\partial}{\partial x_j}(\rho u_i u_j) = -\frac{\partial P}{\partial x_j} + \frac{\partial}{\partial x_j}(\tau_{ij} - \rho\overline{u'_\iota u'_\jmath}) \quad (2)$$

where $\tau_{ij} = \mu\left(\frac{\partial u_i}{\partial x_j} + \frac{\partial u_j}{\partial x_i}\right)$. The turbulence model to close (2) is the kinetic energy of the turbulence and its dissipation rate, and the $\bar{k} - \varepsilon$ model is:

$$\rho\frac{\partial \bar{k}}{\partial t} + \rho u_j\frac{\partial \bar{k}}{\partial x_j} = \frac{\partial}{\partial x_j}\left[\mu\frac{\partial \bar{k}}{\partial x_j} + \frac{\mu_T}{Pr_k}\frac{\partial \bar{k}}{\partial x_j}\right] + \left[2\mu_T S_{ij} - \frac{2}{3}\rho\bar{k}\delta_{ij}\right]\frac{\partial u_i}{\partial x_j} - \rho\varepsilon \quad (3)$$

where $S = \frac{1}{2}\left(\frac{\partial u_i}{\partial x_j} + \frac{\partial u_j}{\partial x_i}\right)$.

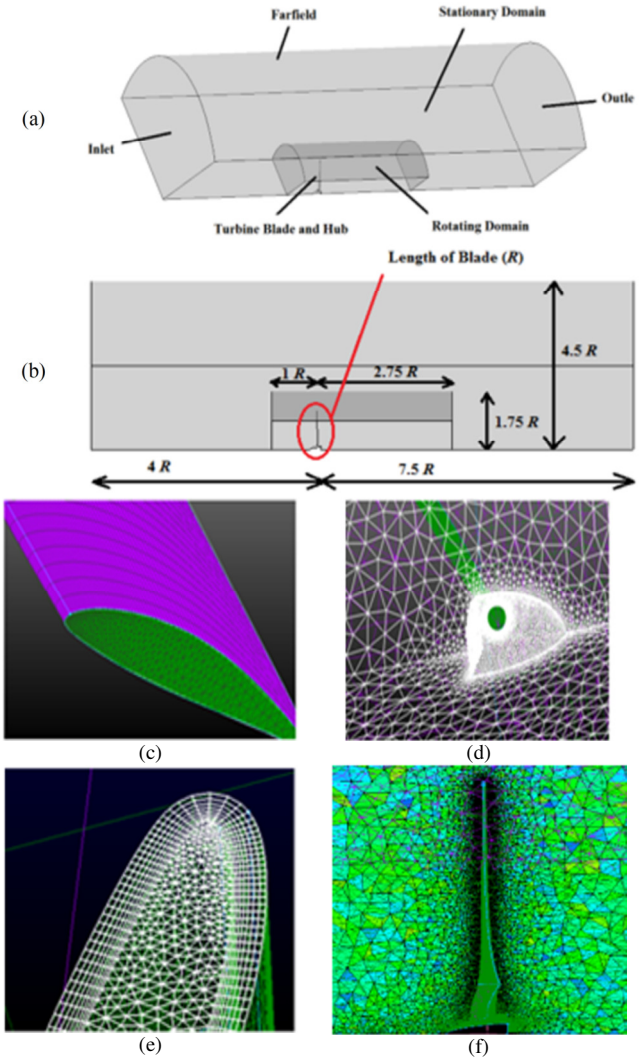

Fig. 2. Computational domain and mesh: (a) computational domain, (b) dimension and layout of the computational domain viewed in ANSYS CFX, (c) quadrilateral cells on the surfaces of the turbine blade, (d) triangular cells on surfaces in the inner section, (e) enlarged look at the leading edge, and (f) tetrahedral volume mesh is applied throughout the computational domain.

$$\rho\frac{\partial \varepsilon}{\partial t} + cu_j\frac{\partial \varepsilon}{\partial x_j} = \frac{\partial}{\partial x_j}\left[\mu\frac{\partial \varepsilon}{\partial x_j} + \frac{\mu_T}{Pr_T}\frac{\partial \varepsilon}{\partial x_j}\right] + C_{\varepsilon 1}\frac{\varepsilon}{k}\left[2\mu_T S_{ij} - \frac{2}{3}\rho\bar{k}\delta_{ij}\right]\frac{\partial u_i}{\partial x_j} - C_{\varepsilon 2}\rho\frac{\varepsilon^2}{\bar{k}} \quad (4)$$

where $\mu_T = C_\mu\,\rho\bar{k}^2/\boldsymbol{\varepsilon}$. Typical values of the model constants C_μ, $C_{\varepsilon 1}$, $C_{\varepsilon 2}$, Pr_k, and Pr_ε can be obtained from previous studies [33], while (3) and (4) are only applicable in the fully turbulent region. The wall function is necessary to relate the near wall velocity to the wall shear stress. Three

turbulence models, *k-ε*, *k-ω,* and *k-ω* SST, have been applied in this research. These models were selected for their ability to effectively handle complex flows around rotating turbine blades. The *k-ε* model provides a balance between accuracy and computational efficiency, while the *k-ω* model captures the near-wall effects, essential for boundary layer analysis. The *k-ω* SST model combines the strengths of both models, improving accuracy in the free-flow and near-wall regions and ensuring reliable predictions under various TSRs. Water flows normally to the y-z plane through the inlet into the steady state domain. The inlet velocity is set according to the local flow velocity, which varies from 0.75 m/s to 1.35 m/s [3]. A reference pressure of 0 Pa is set for the outlet and far fields, as the flow is assumed to be fully developed in front of the two boundaries. The no-slip wall conditions are applied to the hub and blade surfaces and the two surfaces bounding one-third of the domain are identical, so a periodic condition is applied to the surfaces [34].

TABLE III. NUMBER OF MESH ELEMENTS FOR VARIOUS TURBINE SURFACE DIVISIONS

Blade surface mesh dimension (X × Y × Z)	Inner rotating domain mesh number	Overall mesh number	Torque simulation results (Nm)
250 × 30 × 60	2,247,049	2,991,016	8.7293
375 × 45 × 60	3,923,839	4,072,434	9.0666
500 × 60 × 60	4,573,769	4,688,653	9.0121

The inner rotating domain is set to the respective rotational speed with the given TSR value, while the outer domain is set to be stationary. For verification purposes, the rotational speed in terms of TSR used by the benchmark experiment [10] was calculated. After verification, simulations are performed for the designed turbines for East Malaysia to obtain the performance characteristics of the turbines. ANSYS CFX adopts the finite volume method to discretize the governing equation over a collocated grid. Equations (1)-(4) are analyzed as coupled hydrodynamic equations in ANSYS CFX. In addition to the usual convergence criteria, three Cartesian torque components are added to satisfy the criteria. The final results are obtained when the solutions converge to the order of 10^{-6}.

D. Numerical Model Verification

The desired outputs from the simulation are the torques generated by the turbine blade at the respective speeds and the numerical problems are compared with the experimental ones [10]. The power is then derived from the torque and the power coefficient is calculated:

$$C_p = \frac{Generated\ Power}{Rate\ of\ Kinetic\ Energy} = \frac{P}{\frac{1}{2}(\rho\pi R^2 V)V^2} = \frac{P}{\frac{1}{2}\rho\pi R^2 V^3} = \frac{Q\omega}{\frac{1}{2}\rho\pi R^2 V^3} = \frac{Q(TSR)}{\frac{1}{2}\rho\pi R^3 V^2} \quad (5)$$

where P is the power generated, Q is the torque used to rotate the turbine, ρ is the density of the fluid, and V is the incoming flow velocity. A graph of the power coefficient versus TSR is plotted, and the result is compared with the experimental data [10].

E. Hydrodynamic Performance of the Designed Tidal Turbine

After the code validation, simulations are performed to obtain the performance characteristics of the three designed turbine blades. The simulation is carried out for a fixed tidal inflow velocity of 1 m/s subjected to a TSR varying from 3 to 9, while in another parametric study the effect of inflow velocities ranging from 0.75 m/s to 1.35 m/s for a fixed TSR of 5 on the hydrodynamic performance is investigated.

IV. RESULTS AND DISCUSSION

A. Numerical Model Verification

The power coefficients obtained in this theoretical study are compared with the benchmark experimental data [10], as shown in Figure 3. The power coefficient of the turbine increases with the TSR until it is between TSR 5 and TSR 6, beyond which it decreases. The three turbulence models (*k-ε*, *k-ω*, and *k-ω* SST) demonstrate reasonable agreement with the experimental data, with the *k-ε* model exhibiting the most significant correlation, making it the preferable model in all subsequent analyses in this study.

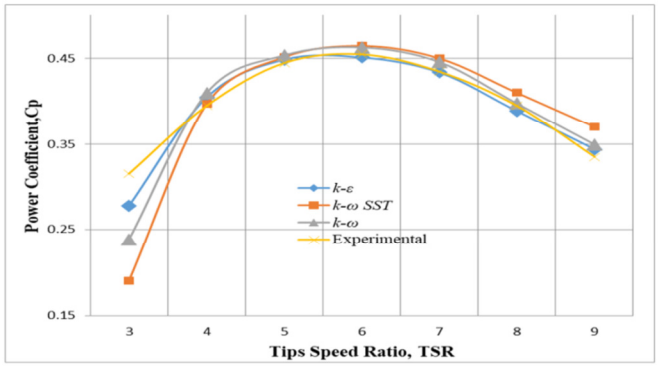

Fig. 3. Power coefficients at various TSRs of the computational model and benchmark experimental data.

As presented in Figures 4-10, the pressure distributions for different TSRs offer insights into the impact of TSR on power generation, with an incoming flow velocity of 1 m/s being constant. As shown in Figure 4, a low-pressure region was formed on the suction side of the blade, while a higher pressure was formed on the pressure side of the turbine blade. As depicted in Figures 5-10, the low-pressure region develops progressively on the suction side of the blade with increasing TSR, increasing the pressure difference between the two sides of the blade. In particular, beyond TSR 5, which is the design TSR shown in Figures 7-10, the high-pressure region begins to grow on the pressure side of the blade, especially at the leading edge. Notably, while the increase in TSR intensifies the high-pressure region at the leading edge of the blade, its net effect on increasing the power coefficient may be diminished because of the amplification of the drag exerted on the turbine blade [32].

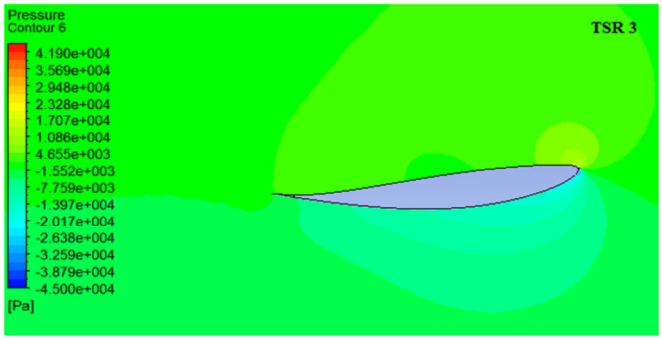

Fig. 4. Pressure contour for TSR 3 at the tip.

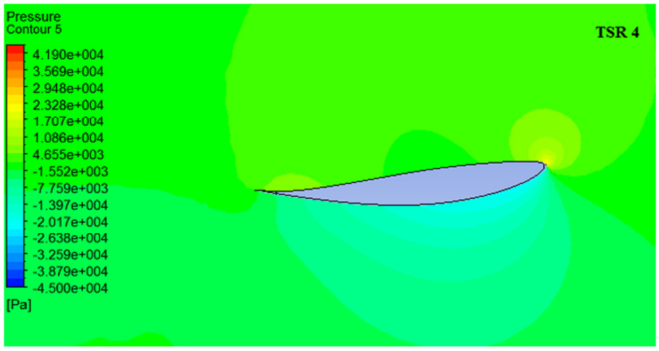

Fig. 5. Pressure contour for TSR 4 at the tip.

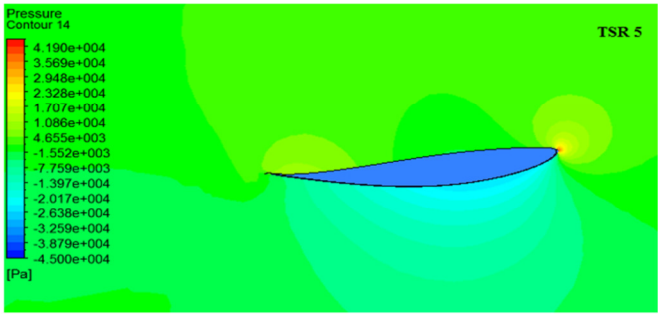

Fig. 6. Pressure contour for TSR 5 at the tip.

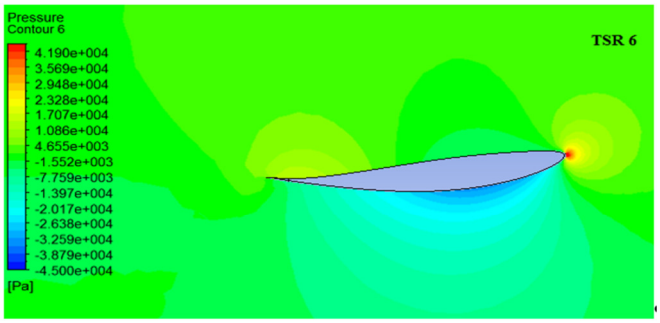

Fig. 7. Pressure contour for TSR 6 at the tip.

The relationship between TSR and turbine performance has practical implications for the deployment of tidal turbines at the three Malaysian sites: Pulau Jambongan, Kota Belud, and Sibu. Each site has unique tidal flow conditions with variations in velocity, depth, and environmental constraints. For example, the optimal TSR range identified in this study (TSR 4-7) suggests that turbines can be tuned to achieve peak performance within the flow conditions of these specific sites.

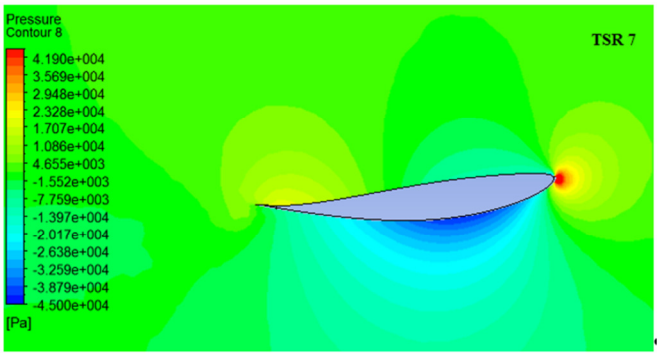

Fig. 8. Pressure contour for TSR 7 at the tip.

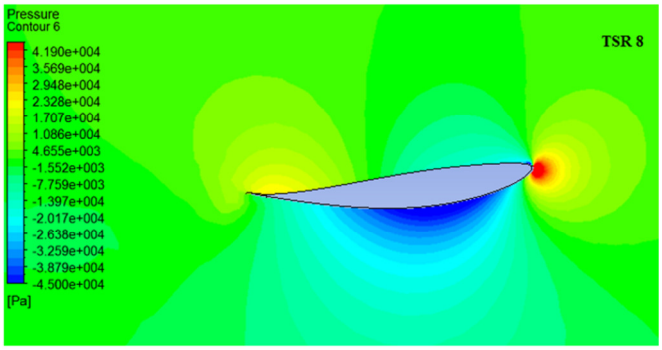

Fig. 9. Pressure contour for TSR 8 at the tip.

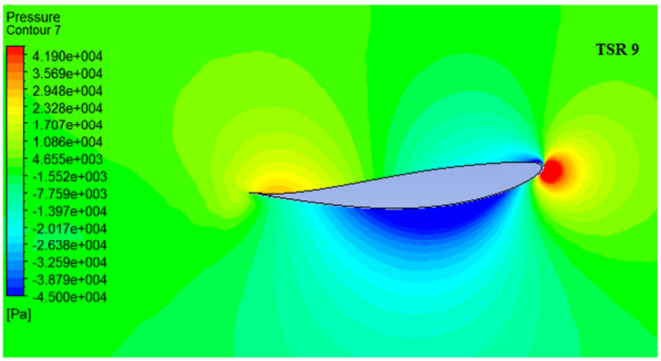

Fig. 10. Pressure contour for TSR 9 at the tip.

In addition, the ability of the turbines to maintain a power coefficient greater than 0.4 over this TSR range indicates performance stability, which is essential for consistent energy production under varying tidal speeds [33]. In real-world applications, fine-tuning the TSR at each site could address challenges, such as maximizing energy capture during peak flow periods and ensuring efficiency during low-speed conditions [34]. This adaptability is particularly relevant for East Malaysia, where tidal currents fluctuate throughout the year. By matching TSR settings to site-specific tidal characteristics, the turbines could provide more stable and efficient power output, supporting the region's sustainable

energy goals and reducing dependence on fossil fuels [35]. As presented in Figures 11-17, flow separation does not occur at all TSRs, demonstrating that the angle of attack decreases as the TSR increases. At TSR 5, the fluid flow angle is at the minimum drag to lift ratio; therefore, it produces maximum power.

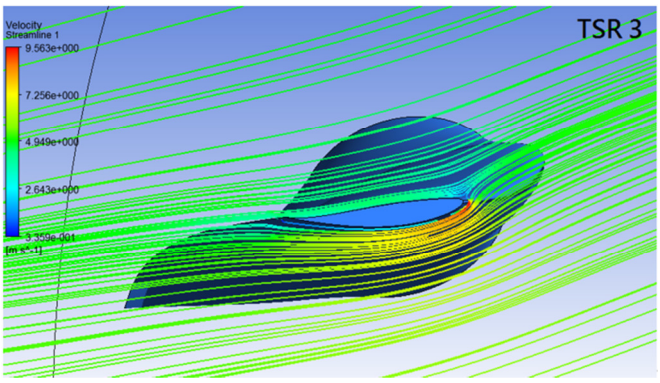

Fig. 11. Velocity and streamline at tip of turbine for TSR 3.

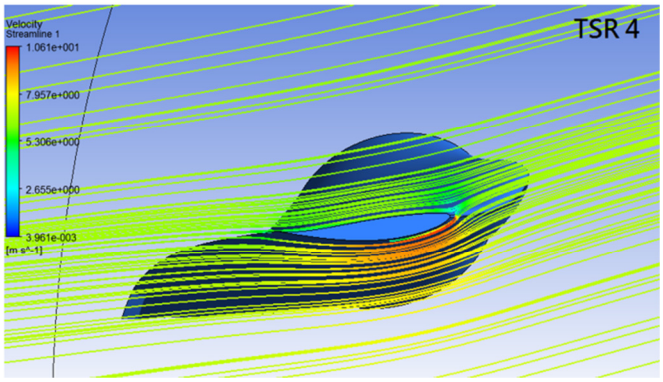

Fig. 12. Velocity and streamline at tip of turbine for TSR 4.

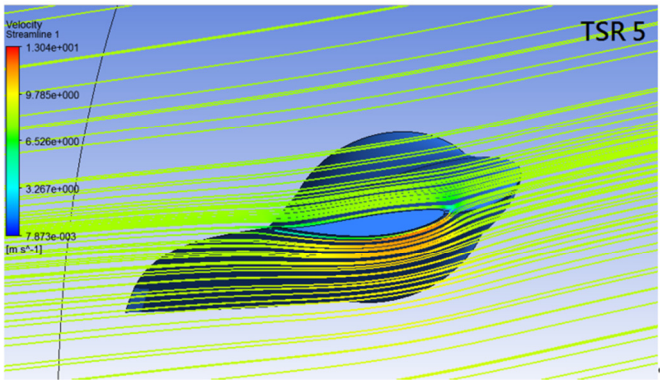

Fig. 13. Velocity and streamline at tip of turbine for TSR 5.

B. Hydrodynamic Performance of Designed Turbines

The hydrodynamic performance of the designed turbines is presented in Figure 18, where a similar pattern to Figure 4 can be seen, with the power coefficients of the turbines increasing as the TSR increases, peaking at the designed TSR and decreasing after the designed TSR.

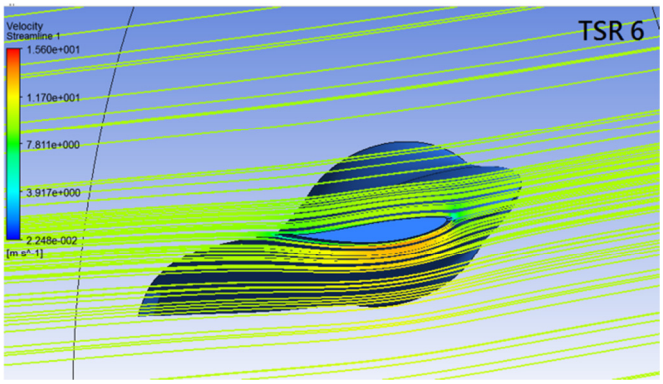

Fig. 14. Velocity and streamline at tip of turbine for TSR 6.

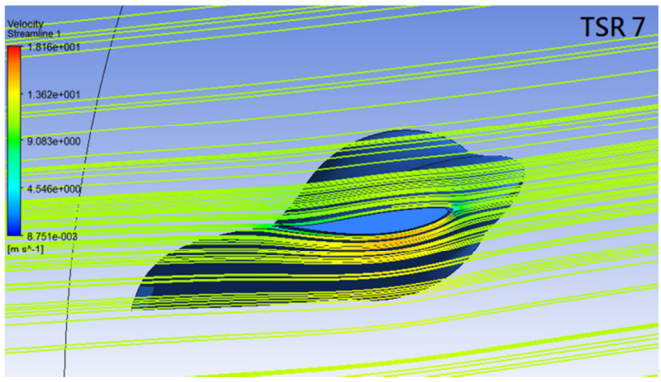

Fig. 15. Velocity and streamline at tip of turbine for TSR 7.

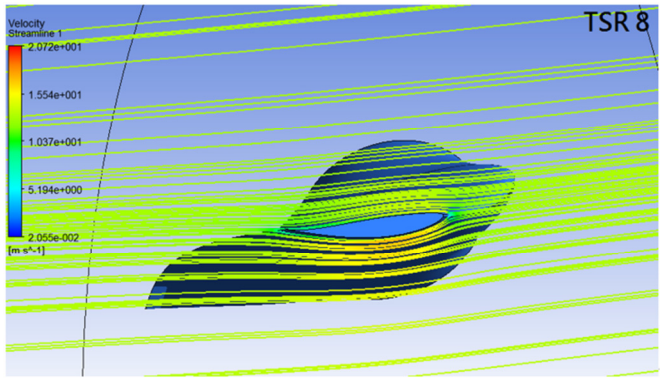

Fig. 16. Velocity and streamline at tip of turbine for TSR 8.

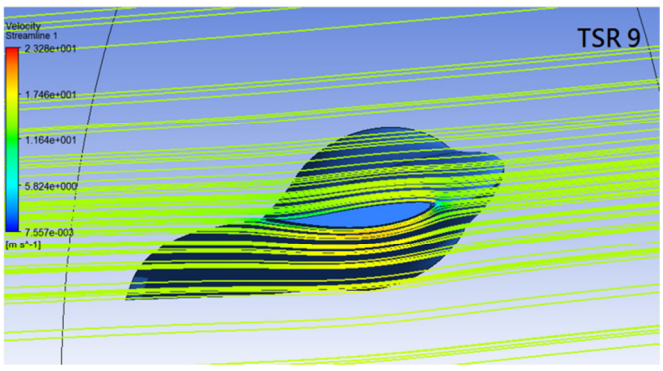

Fig. 17. Velocity and streamline at tip of turbine for TSR 9.

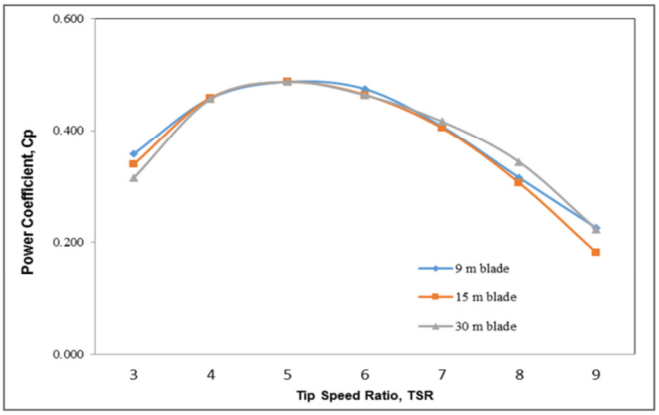

Fig. 18. Hydrodynamic performance characteristic of the 3 designed turbines.

The hydrodynamic characteristics of the turbines are analogous to those of the turbines in the benchmark experiments, as displayed in Table IV. Specifically, the 9-m turbine has a power coefficient greater than 0.4 when rotating from 4.24 RPM to 7.43 RPM. For the other two turbines, a power coefficient greater than 0.4 is attained when the turbine rotates from 2.55 RPM to 4.46 RPM for the 15-meter turbine and from 1.27 RPM to 2.23 RPM for the 30-meter turbine. Figures 19-24 present the absolute pressure contours at the suction side and pressure side of the turbine blade in order to ascertain whether the designed blade is vulnerable to critical pressure levels.

TABLE IV. HYDRODYNAMIC PERFORMANCE OF THE DESIGNED TURBINES

TSR	Rotating speed (RPM)			Power coefficient		
	9-m	15-m	30-m	9-m	15-m	30-m
3	3.18	1.91	0.95	0.358	0.339	0.315
4	4.24	2.55	1.27	0.458	0.459	0.457
5	5.30	3.18	1.59	0.487	0.487	0.487
6	6.37	3.82	1.91	0.475	0.464	0.464

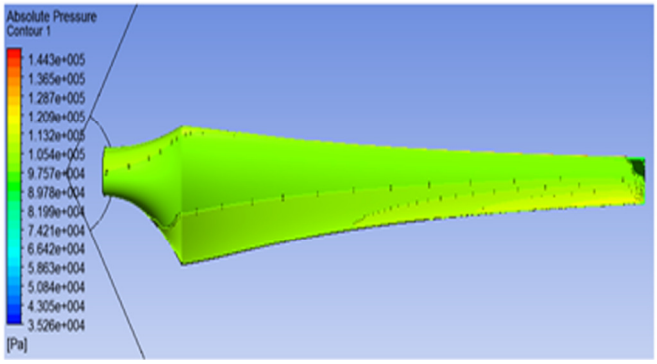

Fig. 19. Absolute pressure for 9-m turbine blade at *TSR* 9 (pressure side).

As shown in Figures 19, 21, higher pressures were encountered at the leading edge of the blades. On the other hand, Figures 20, 22, and 24 demonstrate that the low pressure is focused on the suction side of the blades. This is consistent with the previous results, where the lowest pressure values of all designed turbine blades are above the vapor pressure of water, which is about 3200 Pa at 25 °C.

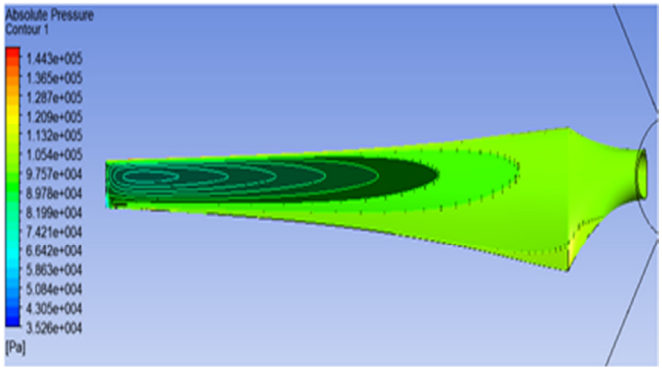

Fig. 20. Absolute pressure for 9-m turbine blade at *TSR* 9 (suction side).

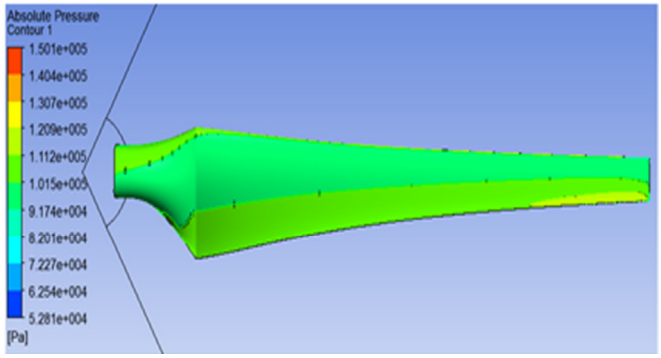

Fig. 21. Absolute pressure for 15-m turbine blade at *TSR* 9 (pressure side).

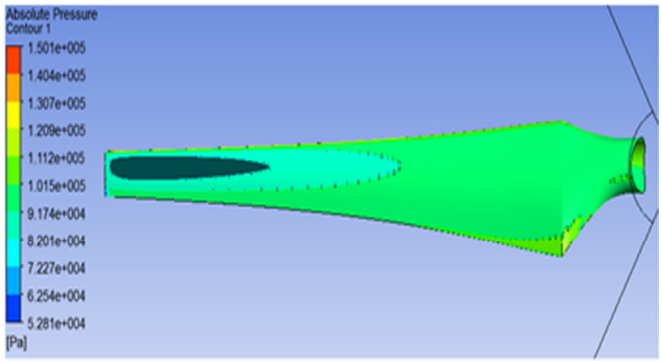

Fig. 22. Absolute pressure for 15-m turbine blade at *TSR* 9 (suction side).

For the designed TSR 5, the simulation was performed for various inflow velocities ranging from 0.75 m/s to 1.35 m/s to obtain the power generated by the turbine. Table V portrays the power produced for all three turbines designed for the three sites in Malaysia. With a power coefficient of 0.4, the turbines can be installed in tidal farm arrangements to generate 8604 GWh of electricity per year in Pulau Jambongan, Kota Belud, and Sibu. The developed CFD methodology allows the calculation of static characteristics, such as power and torque, as a function of the speed of the tidal turbine shaft.

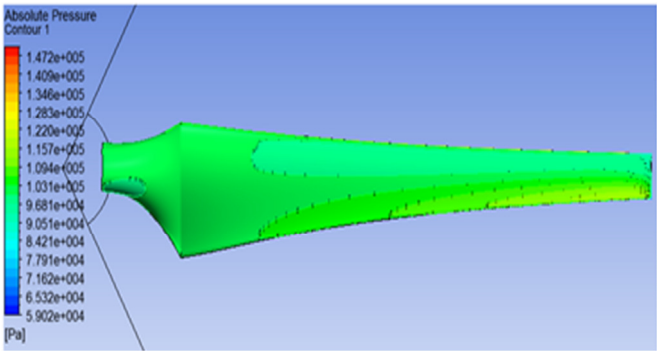

Fig. 23. Absolute pressure for 30-m turbine blade at *TSR* 9 (pressure side).

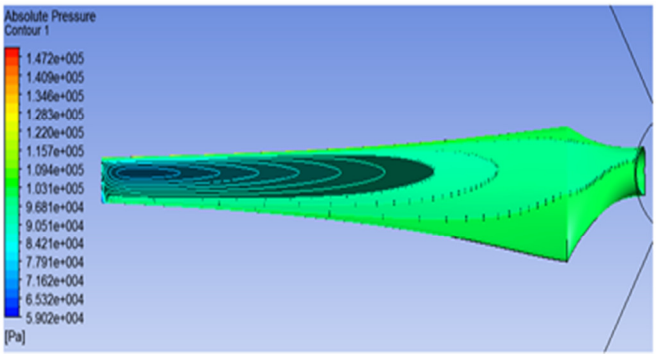

Fig. 24. Absolute pressure for 30-m turbine blade at *TSR* 9 (suction side).

TABLE V. POWER PRODUCED

Stream velocity (m/s)	**Re ($\times 10^6$)**	**9-m Blade**			**15-m Blade**			**30-m Blade**		
		Torque (N·m)	Power (W)	C_p	Torque (N·m)	Power (W)	C_p	Torque (N·m)	Power (W)	C_p
0.75	6.75	20900	26119	0.488	96350	72252	0.486	774000	290329	0.488
0.85	7.65	27000	38246	0.491	124100	105459	0.487	998000	424203	0.490
0.95	8.55	33700	53348	0.491	155150	147394	0.487	1240000	589005	0.487
1.05	9.45	41100	71919	0.490	190000	199483	0.489	1512000	793731	0.486
1.15	10.4	49400	94668	0.491	227950	262099	0.489	1815000	1043453	0.486
1.25	11.3	58300	121449	0.490	268380	335398	0.487	2165000	1352814	0.491
1.35	12.2	68400	153878	0.493	314450	424485	0.489	2510000	1693766	0.488

These parameters are directly determined from the simulation results, where power is calculated using the relationship $P=\omega \times Q$, where ω is the angular velocity and Q is the torque, which, in turn, is calculated based on the force distribution across the turbine blade surfaces. In order to improve power generation from tidal turbines, the high costs of construction, installation, and maintenance of the turbines have to be optimized [36]. Analyzing power and torque output over a range of speeds provides insights that can guide the design and operation of turbines for maximum efficiency.

V. CONCLUSIONS

This study examines the hydrodynamic performance of Tidal Current Turbines especially designed for selected sites in East Malaysia. Using the Computational Fluid Dynamics (CFD) analysis and Blade Element Momentum Theory (BEMT), the performance of tidal turbines was optimized for three key locations: Pulau Jambongan, Kota Belud, and Sibu. The simulation results revealed that a power coefficient of more than 0.4 can be achieved at a Tip Speed Ratio (TSR) between 4 and 7, validating the turbine design for efficient energy production in these locations. The novelty of this research lies in the usage of site-specific tidal velocities and depths to improve turbine performance and sustainability. This approach is a significant step in the adoption of renewable energy technologies to regional characteristics, and provides useful insights into the potential for tidal energy deployment in Malaysia.

ACKNOWLEDGMENT

This study was supported financially by the Ministry of Science, Technology and Innovation Malaysia (MOSTI) under the eScience Fund (06-02-01-SF0172).

REFERENCES

[1] H. Faez Hassan, A. El-Shafie, and O. A. Karim, "Tidal current turbines glance at the past and look into future prospects in Malaysia," *Renewable and Sustainable Energy Reviews*, vol. 16, no. 8, pp. 5707–5717, Oct. 2012, https://doi.org/10.1016/j.rser.2012.06.016.

[2] P. D. Chung, "Evaluation of Reactive Power Support Capability of Wind Turbines," *Engineering, Technology & Applied Science Research*, vol. 10, no. 1, pp. 5211–5216, Feb. 2020, https://doi.org/10.48084/etasr.3260.

[3] Y. S. Lim and S. L. Koh, "Analytical assessments on the potential of harnessing tidal currents for electricity generation in Malaysia," *Renewable Energy*, vol. 35, no. 5, pp. 1024–1032, May 2010, https://doi.org/10.1016/j.renene.2009.10.016.

[4] R. Simbolon, W. Sihotang, and J. Sihotang, "Tapping Ocean Potential: Strategies for integrating tidal and wave energy into national power grids," *GEMOY: Green Energy Management and Optimization Yields*, vol. 1, no. 1, pp. 49–65, Jun. 2024.

[5] S. J. Batinathan, N. C. Yee, and S. Y. Chee, "Exploring Ocean Renewable Energy Potential in Malaysia: A Comprehensive Study of Wind, Wave, and Hybrid Systems," in *Offshore Technology Conference Asia*, Kuala Lumpur, Malaysia, Feb. 2024, https://doi.org/10.4043/34989-MS.

[6] F. Alsebai, H.-S. Kang, O. Yaakob, and M. N. A. W. M. Yazid, "Review of Resources from the Perspective of Wave, Tidal, and Ocean Thermal Energy Conversion," *Journal of Advanced Research in Applied Sciences and Engineering Technology*, vol. 30, no. 3, pp. 127–149, May 2023, https://doi.org/10.37934/araset.30.3.127149.

[7] A. H. Day *et al.*, "Hydrodynamic modelling of marine renewable energy devices: A state of the art review," *Ocean Engineering*, vol. 108, pp. 46–69, Nov. 2015, https://doi.org/10.1016/j.oceaneng.2015.05.036.

[8] M. Nachtane, M. Tarfaoui, I. Goda, and M. Rouway, "A review on the technologies, design considerations and numerical models of tidal current turbines," *Renewable Energy*, vol. 157, pp. 1274–1288, Sep. 2020, https://doi.org/10.1016/j.renene.2020.04.155.

[9] W. Xudong, W. Z. Shen, W. J. Zhu, J. N. Sørensen, and C. Jin, "Shape optimization of wind turbine blades," *Wind Energy*, vol. 12, no. 8, pp. 781–803, 2009, https://doi.org/10.1002/we.335.

[10] A. S. Bahaj, W. M. J. Batten, and G. McCann, "Experimental verifications of numerical predictions for the hydrodynamic performance of horizontal axis marine current turbines," *Renewable Energy*, vol. 32, no. 15, pp. 2479–2490, Dec. 2007, https://doi.org/10.1016/j.renene.2007.10.001.

[11] P. M. Singh and Y.-D. Choi, "Shape design and numerical analysis on a 1 MW tidal current turbine for the south-western coast of Korea," *Renewable Energy*, vol. 68, pp. 485–493, Aug. 2014, https://doi.org/10.1016/j.renene.2014.02.032.

[12] F. O'Rourke, F. Boyle, A. Reynolds, and D. M. Kennedy, "Hydrodynamic performance prediction of a tidal current turbine operating in non-uniform inflow conditions," *Energy*, vol. 93, pp. 2483–2496, Dec. 2015, https://doi.org/10.1016/j.energy.2015.10.078.

[13] W.-H. Lam, L. Chen, and R. Hashim, "Analytical wake model of tidal current turbine," *Energy*, vol. 79, pp. 512–521, Jan. 2015, https://doi.org/10.1016/j.energy.2014.11.047.

[14] B. Mannion, S. B. Leen, and S. Nash, "Development and assessment of a blade element momentum theory model for high solidity vertical axis tidal turbines," *Ocean Engineering*, vol. 197, Feb. 2020, Art. no. 106918, https://doi.org/10.1016/j.oceaneng.2020.106918.

[15] S. Fu, S. Ordonez-Sanchez, R. Martinez, C. Johnstone, M. Allmark, and T. O'Doherty, "Using Blade Element Momentum Theory to Predict the Effect of Wave-Current Interactions on the Performance of Tidal Stream Turbines," *International Marine Energy Journal*, vol. 4, no. 1, pp. 25–36, May 2021, https://doi.org/10.36688/imej.4.25-36.

[16] M. Togneri, G. Pinon, C. Carlier, C. Choma Bex, and I. Masters, "Comparison of synthetic turbulence approaches for blade element momentum theory prediction of tidal turbine performance and loads," *Renewable Energy*, vol. 145, pp. 408–418, Jan. 2020, https://doi.org/10.1016/j.renene.2019.05.110.

[17] M. L. Ruh and J. T. Hwang, "Fast and Robust Computation of Optimal Rotor Designs Using Blade Element Momentum Theory," *AIAA Journal*, vol. 61, no. 9, pp. 4096–4111, Sep. 2023, https://doi.org/10.2514/1.J062611.

[18] U. Boatto, P. A. Bonnet, F. Avallone, and D. Ragni, "Assessment of Blade Element Momentum Theory-based engineering models for wind turbine rotors under uniform steady inflow," *Renewable Energy*, vol. 214, pp. 307–317, Sep. 2023, https://doi.org/10.1016/j.renene.2023.04.050.

[19] O. I. Abdullah, M. S. Ghanim, M. J. Jweeg, H. S. Sultan, and A. M. Abed, "A study on the wind blade performance using blade element momentum theory," *AIP Conference Proceedings*, vol. 2776, no. 1, Apr. 2023, Art. no. 050005, https://doi.org/10.1063/5.0135950.

[20] F. Zilic de Arcos, A. Wimshurst, R. H. J. Willden, G. Pinon, and C. R. Vogel, "A CFD Study on High-Thrust Corrections for Blade Element Momentum Models," *Wind Energy*, vol. 27, no. 10, 2024, Art. no. e2937, https://doi.org/10.1002/we.2937.

[21] W. Yan, X. Tian, J. Zhou, and K. Zhang, "Research on the Calculation Method of Propeller 1P Loads Based on the Blade Element Momentum Theory," *Aerospace*, vol. 11, no. 5, May 2024, Art. no. 332, https://doi.org/10.3390/aerospace11050332.

[22] D. V. Lieder, J. Oldeweme, B. Kirsch, and J. Friedichs, "Comparison of Blade Element Momentum and Lifting Line Models for Preliminary Propeller Design," in *AIAA Aviation Forum and ASCEND 2024*, Las Vegas, NV, USA, https://doi.org/10.2514/6.2024-4555.

[23] I. Malael and V. Dragan, "Numerical and Experimental Efficiency Evaluation of a Counter-Rotating Vertical Axis Wind Turbine," *Engineering, Technology & Applied Science Research*, vol. 8, no. 4, pp. 3282–3286, Aug. 2018, https://doi.org/10.48084/etasr.2231.

[24] M. Ye, H.-C. Chen, and A. Koop, "Verification and validation of CFD simulations of the NTNU BT1 wind turbine," *Journal of Wind Engineering and Industrial Aerodynamics*, vol. 234, Mar. 2023, Art. no. 105336, https://doi.org/10.1016/j.jweia.2023.105336.

[25] A. Abdelkhalig, M. Elgendi, and M. Y. E. Selim, "Review on validation techniques of blade element momentum method implemented in wind turbines," *IOP Conference Series: Earth and Environmental Science*, vol. 1074, no. 1, Aug. 2022, Art. no. 012008, https://doi.org/10.1088/1755-1315/1074/1/012008.

[26] J. F. Manwell, J. G. McGowan, and A. L. Rogers, *Wind Energy Explained: Theory, Design and Application*, 2nd edition. Chichester, West Sussex, UK: Wiley, 2010.

[27] A. S. Bahaj and L. Myers, "Analytical estimates of the energy yield potential from the Alderney Race (Channel Islands) using marine current energy converters," *Renewable Energy*, vol. 29, no. 12, pp. 1931–1945, Oct. 2004, https://doi.org/10.1016/j.renene.2004.02.013.

[28] A. F. Molland, A. S. Bahaj, J. R. Chaplin, and W. M. J. Batten, "Measurements and predictions of forces, pressures and cavitation on 2-D sections suitable for marine current turbines," *Proceedings of the Institution of Mechanical Engineers, Part M: Journal of Engineering for the Maritime Environment*, vol. 218, no. 2, pp. 127–138, Jun. 2004, https://doi.org/10.1243/1475090041651412.

[29] A. L. Pape and J. Lecanu, "3D Navier–Stokes computations of a stall-regulated wind turbine," *Wind Energy*, vol. 7, no. 4, pp. 309–324, 2004, https://doi.org/10.1002/we.129.

[30] A. S. Bahaj, A. F. Molland, J. R. Chaplin, and W. M. J. Batten, "Power and thrust measurements of marine current turbines under various hydrodynamic flow conditions in a cavitation tunnel and a towing tank," *Renewable Energy*, vol. 32, no. 3, pp. 407–426, Mar. 2007, https://doi.org/10.1016/j.renene.2006.01.012.

[31] D. Anderson, J. C. Tannehill, R. H. Pletcher, R. Munipalli, and V. Shankar, *Computational Fluid Mechanics and Heat Transfer*, 4th ed. Boca Raton, Fl, USA: CRC Press, 2020.

[32] O. Yilmaz, "Increasing power coefficient of small wind turbine over a wide tip speed range by determining proper design tip speed ratio and number of blades," *Proceedings of the Institution of Mechanical Engineers, Part C: Journal of Mechanical Engineering Science*, vol. 236, no. 23, pp. 11211–11230, Dec. 2022, https://doi.org/10.1177/09544062221110396.

[33] Y. Zheng, W. Yang, K. Wei, Y. Chen, and H. Zou, "Enhancing Efficiency and Reliability of Tidal Stream Energy Conversion through Swept-Blade Design," *Energies*, vol. 17, no. 2, Jan. 2024, Art. no. 334, https://doi.org/10.3390/en17020334.

[34] V. Pettas, "Wind turbine operational optimization considering revenue and fatigue objectives," Ph.D. dissertation, Institute of Aircraft Design, University of Stuttgart, Stuttgart, Germany, 2024.

[35] R. O'Connell *et al.*, "The Integration of Tools for the Techno-Economic Evaluation of Fixed and Floating Tidal Energy Deployment in the Irish Sea," *Energies*, vol. 16, no. 22, Jan. 2023, Art. no. 7526, https://doi.org/10.3390/en16227526.

[36] J. Xu *et al.*, "DLFSI: A deep learning static fluid-structure interaction model for hydrodynamic-structural optimization of composite tidal turbine blade," *Renewable Energy*, vol. 224, Apr. 2024, Art. no. 120179, https://doi.org/10.1016/j.renene.2024.120179.